STABILITY ANALYSIS WITH UNCERTAINTY FOR TWIST DRILLING

Tony Schmitz[1,2], Michael Gomez[1,2], Andrew Honeycutt[2], Jaydeep Karandikar[2], Jongyoup Shim[3], Seung-Kook Ro[3], and Jooho Hwang[3]
[1]Mechanical, Aerospace, and Biomedical Engineering
University of Tennessee, Knoxville
Knoxville, TN 37996, USA
[2]Energy and Transportation Science Division
Oak Ridge National Laboratory
Oak Ridge, TN 37830, USA
[3]Advanced Manufacturing Systems Research Division
Korea Institute of Machinery & Materials
Yuseong-gu, Daejeon 34103, Korea

INTRODUCTION[1]

Hole making is an important machining activity for the aerospace, automotive, ship building, and biomedical industries, to name a few. The associated materials of interest are metal alloys, reinforced composites, polymers, bone, and others [1-5]. Mechanical techniques include twist drilling, vibration assisted twist drilling, ultrasonic machining, and rotary ultrasonic machining [1]. Among these, twist drilling is the most prevalent technique with process parameters that include spindle speed, feed rate, drill diameter and geometry, drill material, drill coating, work material, pilot hole diameter, and coolant/lubricant application method and amount.

One limitation to hole quality, drill life, and material removal rate in twist drilling is chatter, a self-excited vibration caused by regeneration of waviness, or the overcutting of the previously machined surface with a spindle speed-dependent time delay [6]. In milling, regeneration of waviness causes chip thickness variation due to lateral bending of the end mill and other vibration modes that give deflection perpendicular to the tool axis (i.e., the feed direction in peripheral end milling) [7-8]. In drilling, on the other hand, regeneration occurs due to vibrations in the axial (feed) direction. Axial deflection of the twist drill during material removal causes chip thickness variation which, in turn, can lead to self-excited vibration depending on the combination of spindle speed and chip width (i.e., the difference between the twist drill diameter and pilot hole diameter, if applicable). A primary mechanism for this axial vibration is torsional-axial coupling due to the drill geometry. The helical drill shape leads to beam twist (about the axis) when an axial force is applied and, conversely, an axial deflection when a torque is applied [9].

While prior modeling efforts differ in approach and solution technique, they each treat the drilling process as deterministic. However, it is well-understood that the inputs to these models, as well as the analyses themselves, are uncertain. To enable a predictive capability, it is essential to consider these uncertainties and subsequently provide uncertain (probabilistic) model outputs. The contribution of this paper is to present the first uncertainty analysis for drilling stability using the frequency-domain model presented in [6] to identify the relationships between uncertainties in the measured inputs and output (i.e., the stability map). Due to the nonlinear nature of the stability model, Monte Carlo simulation is implemented to complete the uncertainty propagation. Experiments are also performed to compare with predictions and stability limit uncertainty bounds.

The paper is organized as follows. First, as a convenience to the reader, the twist drilling stability algorithm described in [6] is detailed. Second, the Monte Carlo uncertainty analysis is

described. Third, experimental results are presented. Finally, conclusions are discussed.

FREQUENCY-DOMAIN STABILITY ANALYSIS

Axial feed of a twist drill into the workpiece causes the chip thickness to increase. The thrust force (aligned with the drill axis, *z*) required to shear away this chip is:

$$F_z = -C_2 bh, \tag{1}$$

where C_2 depends on the drill geometry and work material, h is the chip thickness and b is the chip width (i.e., the difference between the twist drill diameter and the pilot hole diameter, if applicable). The associated torque is:

$$M_z = -C_1 bhR_{av}, \tag{2}$$

where C_1 also depends on the drill geometry and work material and R_{av} is the average radius of the force. With vibration in the axial direction, the chip thickness varies and its instantaneous value depends on the mean (commanded) value, the current vibration, and the previous cutting edge vibration at the same drill rotational angle:

$$h = h_{av} + z - z(t - \tau), \tag{3}$$

where h_{av} is the feed per cutting edge (or flute, two flutes total for twist drills) and τ is the time delay between flutes. This time delay serves as the mechanism for regenerative chatter. Although the twist drill is stiff in the *z* (axial) direction, its geometry leads to coupling between the torsional and axial vibration modes. As noted, an axial force causes the beam to twist and a torque causes it to change length.

The second-order, time delay differential equation of motion for the drilling process can be written as:

$$M\ddot{u} + C\dot{u} + Ku = F, \tag{4}$$

where u is the generalized coordinate that includes translations in the *x*, *y*, and *z* directions and rotations, θ, about the *z* axis:

$$u = \begin{bmatrix} x_1 & x_2 & \cdots & x_N & y_1 & y_2 & \cdots & y_N \\ z_1 & z_2 & \cdots & z_N & \theta_1 & \theta_2 & \cdots & \theta_N \end{bmatrix}^T. \tag{5}$$

and the subscripts indicate the axial location (*N* is the tip). Returning to Eq. 4, F is the generalized force:

$$F = \begin{bmatrix} F_{x1} & F_{x2} & \cdots & F_{xN} & F_{y1} & F_{y2} & \cdots & F_{yN} \\ F_{z1} & F_{z2} & \cdots & F_{zN} & M_{z1} & M_{z2} & \cdots & M_{zN} \end{bmatrix}^T. \tag{6}$$

In Eq. 6, F_x and F_y are the unbalanced forces in the *x* and *y* directions and the other entries were defined in Eqs. 1 and 2. To convert from physical to modal parameters using modal analysis, the mode shapes are required. Let ψ_n be a vibration mode (mode number *n*) that can contain contributions from bending, torsion, and axial deformations of the twist drill.

$$\psi_n = \begin{bmatrix} q_{1n} & q_{2n} & \cdots & q_{Nn} & r_{1n} & r_{2n} & \cdots & r_{Nn} \\ s_{1n} & s_{2n} & \cdots & 1 & \alpha_{1n} & \alpha_{2n} & \cdots & \alpha_{Nn} \end{bmatrix}^T. \tag{7}$$

$$u = \psi_n p. \tag{8}$$

Substitution of Eq. 8 into Eq. 4 yields:

$$M\psi_n\ddot{p} + C\psi_n\dot{p} + K\psi_n p = F. \tag{9}$$

Pre-multiplying both sides by ${\psi_n}^T$ gives:

$${\psi_n}^T M\psi_n\ddot{p} + {\psi_n}^T C\psi_n\dot{p} + {\psi_n}^T K\psi_n p = {\psi_n}^T F. \tag{10}$$

Considering excitation at the twist drill tip only, Eq. 6 simplifies to:

$$F = \begin{bmatrix} 0 & 0 & \cdots & F_{xN} & 0 & 0 & \cdots & F_{yN} \\ 0 & 0 & \cdots & F_{zN} & 0 & 0 & \cdots & M_{zN} \end{bmatrix}^T. \tag{11}$$

Applying the orthogonality of eigenvectors and assuming proportional damping [34], the equation of motion in modal coordinates is:

$$M_q\ddot{q} + C_q\dot{q} + K_q q = {\psi_n}^T F. \tag{12}$$

Considering only the torsional-axial contributions to Eq. 7, the mode shape simplifies to:

$$\psi_n = \begin{bmatrix} 0 & 0 & \cdots & 0 & 0 & 0 & \cdots & 0 \\ 0 & 0 & \cdots & 1 & \alpha_{1n} & \alpha_{2n} & \cdots & \alpha_{Nn} \end{bmatrix}^T \tag{13}$$

In this case, the generalized modal force vector simplifies to:

$${\psi_n}^T F = F_{zN} + \alpha_{Nn} M_{zN}, \tag{14}$$

where α_{Nn} serves as a coupling parameter that relates the torque to the torsional-axial vibration mode. The simplified mode shape in Eq. 13

enables the chip thickness equation (Eq. 3) to be written in modal coordinates by direct substitution:

$$h = h_{av} + q - q(t-\tau). \quad (15)$$

Substituting Eqs. 1 and 2 in Eq. 14 yields:

$$F_{zN} + \alpha_{Nn} M_{zN} = -C_2 bh - \alpha_{Nn} C_1 bh R_{av}. \quad (16)$$

Rewriting Eq. 16 gives:

$$F_{zN} + \alpha_{Nn} M_{zN} = -(C_2 + \alpha_{Nn} C_1 R_{av}) bh = -\left(\frac{C_1}{C_2} + \alpha_{Nn} C_1 R_{av}\right) C_1 bh. \quad (17)$$

Substituting $\beta = \frac{C_1}{C_2}$ and inserting the chip thickness from Eq. 15 yields:

$$F_{zN} + \alpha_{Nn} M_{zN} = -\beta C_1 b\big(h_{av} + q - q(t-\tau)\big). \quad (18)$$

Considering only the time-varying component of Eq. 18, the new equation of motion is:

$$M_q \ddot{q} + C_q \dot{q} + K_q q = -\beta C_1 b\big(q - q(t-\tau)\big). \quad (19)$$

Converting Eq. 19 to the frequency domain using the Fourier transform, the result is:

$$Q(\omega)\big(-M_q\omega^2 + i\omega C_q + K_q\big) = -\beta C_1 b Q(\omega)(1 - e^{-i\omega_c \tau}), \quad (20)$$

where ω_c is the chatter frequency. Substituting the torsional-axial mode receptance, $H_n(\omega) = \big(-M_q\omega^2 + i\omega C_q + K_q\big)^{-1}$, in Eq. 20 gives:

$$Q(\omega) = -\beta C_1 H_n(\omega) b Q(\omega)(1 - e^{-i\omega_c \tau}). \quad (21)$$

Moving all terms to the left hand side of Eq. 21 and factoring yields:

$$Q(\omega)\left(1 + \beta C_1 H_n(\omega) b(1 - e^{-i\omega_c \tau})\right) = 0. \quad (22)$$

The (τ, b) pairs that define the stability limit satisfy the characteristic equation:

$$1 + \beta C_1 H_n(\omega) b(1 - e^{-i\omega_c \tau}) = 0. \quad (23)$$

The torsional-axial mode receptance is complex-valued, i.e., $H_n(\omega) = \mathrm{Re}(H_n) + i\mathrm{Im}(H_n)$. Additionally, the Euler identity can be used to rewrite the exponential term, $e^{-i\omega_c \tau} = \cos\omega_c\tau - i\sin\omega_c\tau$. Substituting both in Eq. 23 gives:

$$1 + \beta C_1\big(\mathrm{Re}(H_n) + i\mathrm{Im}(H_n)\big) b(1 - \cos\omega_c\tau + i\sin\omega_c\tau) = 0. \quad (24)$$

Expanding Eq. 24 results in:

$$1 + \beta C_1 b\big((\mathrm{Re}(H_n) - \mathrm{Re}(H_n)\cos\omega_c\tau + i\mathrm{Re}(H_n)\sin\omega_c\tau) + i(\mathrm{Im}(H_n) - \mathrm{Im}(H_n)\cos\omega_c\tau + i\mathrm{Im}(H_n)\sin\omega_c\tau)\big) = 0. \quad (25)$$

Both the real and imaginary parts of Eq. 25 must equate to zero. The real part is:

$$1 + \beta C_1 b(\mathrm{Re}(H_n) - \mathrm{Re}(H_n)\cos\omega_c\tau - \mathrm{Im}(H_n)\sin\omega_c\tau) = 0. \quad (26)$$

The imaginary part of Eq. 25 is:

$$\beta C_1 b(\mathrm{Re}(H_n)\sin\omega_c\tau + \mathrm{Im}(H_n) - \mathrm{Im}(H_n)\cos\omega_c\tau) = 0. \quad (27)$$

Rewriting Eq. 27 gives:

$$\frac{\mathrm{Im}(H_n)}{\mathrm{Re}(H_n)} = \frac{-\sin\omega_c\tau}{1-\cos\omega_c\tau} = \tan\phi, \quad (28)$$

which relates the chatter frequency and the time delay. Also, from the receptance definition, the ratio of the imaginary part to the real part is the tangent of the phase, ϕ. Returning to Eq. 26 and solving for the limiting chip width, b_{lim}:

$$b_{lim} = \frac{-1}{\beta C_1(\mathrm{Re}(H_n)(1-\cos\omega_c\tau) - \mathrm{Im}(H_n)\sin\omega_c\tau)}. \quad (29)$$

Rewriting the denominator gives:

$$b_{lim} = \frac{-1}{\beta C_1 \mathrm{Re}(H_n)\left((1-\cos\omega_c\tau) - \frac{\mathrm{Im}(H_n)}{\mathrm{Re}(H_n)}\sin\omega_c\tau\right)}. \quad (30)$$

Substituting Eq. 28 into Eq. 30 gives:

$$b_{lim} = \frac{-1}{\beta C_1 \mathrm{Re}(H_n)\left((1-\cos\omega_c\tau) + \frac{\sin\omega_c\tau}{1-\cos\omega_c\tau}\sin\omega_c\tau\right)}. \quad (31)$$

Equation 31 simplifies to:

$$b_{lim} = \frac{-1}{2\beta C_1 \mathrm{Re}(H_n)}. \quad (32)$$

Because β is negative, only the positive portion of the frequency-dependent $\mathrm{Re}(H_n)$ is considered (i.e., $\mathrm{Re}(H_n) > 0$) in order to obtain positive limiting chip width values. Returning to Eq. 28, the sine and cosine terms can be rewritten using the

double angle trigonometric formulas provided in Eqs. 33 and 34.

$$\sin \omega_c \tau = 2 \sin \frac{\omega_c \tau}{2} \cos \frac{\omega_c \tau}{2} \quad (33)$$

$$\cos \omega_c \tau = \cos^2 \frac{\omega_c \tau}{2} - \sin^2 \frac{\omega_c \tau}{2} \quad (34)$$

Substituting these formulas in Eq. 28 yields:

$$\frac{\mathrm{Im}(H_n)}{\mathrm{Re}(H_n)} = \frac{-2 \sin \frac{\omega_c \tau}{2} \cos \frac{\omega_c \tau}{2}}{1 - \cos^2 \frac{\omega_c \tau}{2} + \sin^2 \frac{\omega_c \tau}{2}} = \frac{-2 \sin \frac{\omega_c \tau}{2} \cos \frac{\omega_c \tau}{2}}{2 \sin^2 \frac{\omega_c \tau}{2}} = \frac{-\cos \frac{\omega_c \tau}{2}}{\sin \frac{\omega_c \tau}{2}} = \cot \frac{-\omega_c \tau}{2}. \quad (35)$$

The final expression from Eq. 35 can be written as:

$$\tan \left(\frac{\pi}{2} + \frac{\omega_c \tau}{2} \pm l\pi \right). \quad (36)$$

Equating Eq. 36 to the right hand side of Eq. 28 gives:

$$\frac{\pi}{2} + \frac{\omega_c \tau}{2} \pm l\pi = \phi. \quad (37)$$

Solving Eq. 37 for $\omega_c \tau$ results in:

$$\omega_c \tau = 2\phi - \pi \mp 2l\pi. \quad (38)$$

Because twist drills have two flutes, the spindle speed (in rpm) is written as:

$$\Omega = \frac{60}{2\tau} = \frac{60}{2} \frac{\omega_c}{2\phi - \pi \mp 2l\pi} = \frac{60\omega_c}{4\phi - 2\pi \mp 4l\pi} = \frac{60\omega_c}{4\phi + 2\pi(2l-1)}, \quad (39)$$

where l = 1, 2, 3, … is the integer number of oscillations in the surface profile between cutting edges (at the bottom of the drilled hole) and the negative values for $\mp 4l\pi$ were selected to obtain positive spindle speeds. The stability map is finally obtained by plotting the spindle speed (Eq. 39) versus the limiting chip width (Eq. 32) for l = 1, 2, 3, …. The stability limit is determined from the smallest b_{lim} value at each spindle speed considering all stability lobes simultaneously.

MONTE CARLO SIMULATION

The primary steps for Monte Carlo simulation are: 1) define the inputs and their probability distributions; 2) randomly select a value for each input from the probability distributions; 3) perform a deterministic computation using the inputs to find the output(s); and 4) aggregate the results after many repetitions for a statistical analysis. In this study, the inputs were selected to be: the modal stiffness, k, modal damping ratio, ζ, and natural frequency, f_n, for the torsional-axial vibration mode of the twist drill when clamped in the holder and spindle; and the torque coefficient C_1. For the remaining parameters, it was assumed that $C_2 = \frac{C_1}{3}$ and $\alpha_{Nn} R_{av} = -3.2$. For the former, this means that the tangential force component is three times larger than the axial force component. For the latter, the negative sign indicates that the twist drill extends as it unwinds and that the torsional deflection is 3.2 times the axial deflection at the drill tip. Both assumptions follow the analysis from [6].

Mean values for the uncertain inputs, {k, ζ, f_n, C_1}, were selected based on testing. Standard deviations were chosen using testing, experience, and process knowledge; a normal distribution was assumed for each input. Additional details are provided in Section 4. The output was the stability map, which identifies the stability boundary as a function of spindle speed. The algorithm described in Section 2 was used to generate this map over multiple iterations with inputs randomly sampled from the pre-defined normal distributions. The speed-dependent variation in the collection of output stability boundaries was then analyzed to determine the associated confidence intervals.

RESULTS

The experimental setup included:

- 9.525 mm diameter, 135 deg split point, 152.4 mm long, high-speed steel (cobalt oxide coating) twist drill with a 116 mm extension
- collet holder with CAT-40 spindle interface
- Haas TM-1P CNC machining center
- 6061-T6 aluminum workpiece
- Kistler 9257B cutting force dynamometer.

The workpiece was bolted to the dynamometer, which was mounted on the machine table, to enable thrust (z) force measurement during drilling trials.

Separate drilling tests were completed for a range of feed per tooth values to define $C_1 = 2.69 \times 10^8$ N/m^2 as described in [6]. For these tests, it is important to understand that the drill geometry varies with radial position along the cutting edge. In this study, blind hole stability was evaluated, so blind holes were selected to determine C_1.

However, to generalize predictions, pilot hole drilling should also be completed. Because the force model coefficients changes with pilot hole diameter, a mean value can be selected. However, this increases uncertainty.

Frequency response functions, or FRFs, were measured by impact testing, where a small hammer (PCB model 086E80) was used to excite the drill tip and an accelerometer (PCB model 352C23) was used to measure the vibration response; both time-domain signals were collected and converted to the frequency-domain using MLI's MetalMax TXF software. To identify the required torsional-axial mode, three measurements were performed. First, the FRF in the axial direction, where the accelerometer was mounted at the drill tip with its sensitive direction aligned (as much as possible) with the drill axis. The hammer was used to tap the drill adjacent to the accelerometer in the axial direction. Due to the angled lips and small surface area, the tap direction was not perfectly aligned with the drill axis, nor perfectly consistent.

Due to the imperfect alignment of both the hammer and accelerometer with the drill axis, the drill's bending modes (in the lateral direction) were also excited. To distinguish between the torsional-axial and bending modes, two additional measurement setups were used. For the lateral direction FRF measurements, the drill was impacted on the margin perpendicular to the drill axis and nominally on its centerline. The accelerometer was attached on the opposite margin (directly across from the hammer strike), where the accelerometer measurement axis was colinear with the force vector (again, with some alignment uncertainty) to ideally excite only bending modes.

For the torsion measurements, the drill was excited at the outer edge of the cutting lip to intentionally cause rotation about the drill axis. The accelerometer was placed on the outer edge of the cutting lip with its measurement axis parallel to, but offset from, the force vector and pointing in the opposite direction. This setup inherently excites both bending and torsional modes. The three measurement results are superimposed in Fig. 1. It is seen that the lateral FRF primarily excites the first bending mode with a natural frequency of 500 Hz; however, a second mode at 535 Hz is also observed. The torsion FRF, on the other hand, primarily excites the torsional response at 535 Hz although the 500 Hz bending mode is still seen with a smaller magnitude. The axial FRF shows both modes, but it is now possible to isolate the peak at 535 Hz as the torsional-axial mode to be used for the stability analysis. The mode is inverted due to the accelerometer orientation/strike direction and relationship between axial and torsional deflection. A modal fit provided the following values: $k = 6\times10^7$ N/m, $\zeta = 0.005$, and $f_n = 540$ Hz (note that the measurement was compensated for the accelerometer mass, so the modeled natural frequency is higher than the measured natural frequency in Fig. 1 [35]).

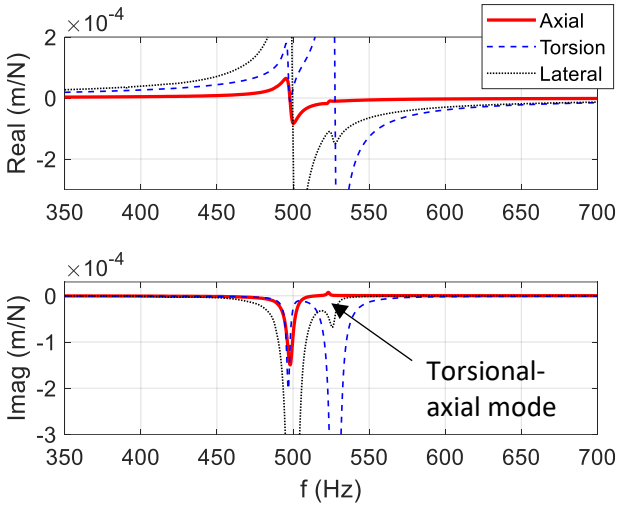

FIGURE 1: FRF measurement results.

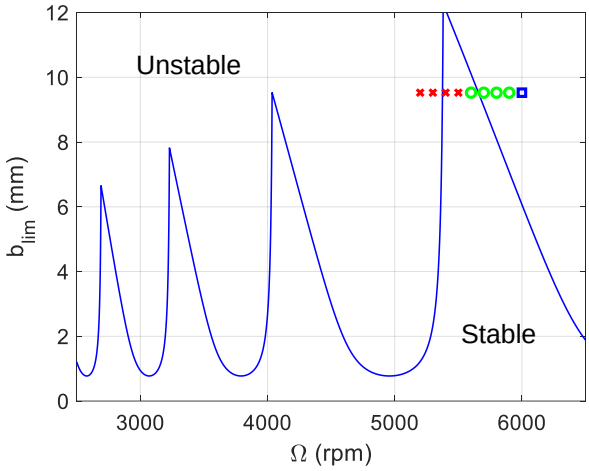

FIGURE 2: Drilling stability map with experimental results, where an × represents an unstable (chatter) result, a circle is for a stable result, and a square indicates marginal stability.

Drilling experiments were completed at spindle speeds from 5200 rpm to 6000 rpm in 100 rpm increments. A 3.175 mm diameter center drill was used to set each hole location prior to drilling and avoid bending vibrations during the hole entry transient. No pilot hole was used so the chip width was equal to the 9.525 mm drill diameter at steady-state. The feed per flute was 0.152 mm in all cases. The stability map and test results are displayed in Fig. 2. The corresponding chatter frequency, f_c, versus spindle speed plot is provided in Fig. 3. The flute passing frequency line (equal to the product of the spindle speed and number of flutes, 2) is also included to identify the stable cuts, where no chatter frequency was present.

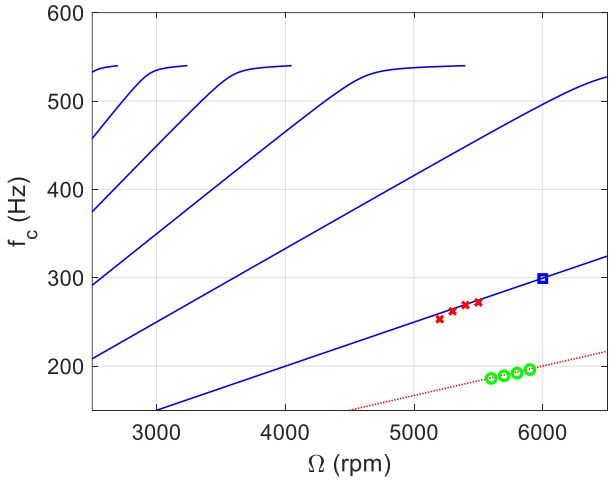

FIGURE 3: Chatter frequency variation with spindle speed (solid lines). Experimental results are included, as well as the flute passing frequency (dotted line).

The Monte Carlo simulation was next completed using the input mean and standard deviation values listed in Table 1. The standard deviation is presented as a percent of the mean value in each case. These percentages were selected based on the authors' experiences with the input parameter measurements. For example, in the axial direct FRF measurement, it is challenging to apply the force and measure the response in the drill's axial direction. Therefore, large uncertainty percentages were assigned to the modal stiffness and damping for the fit to the torsional-axis mode. A much smaller percent was applied to the natural frequency, however, because it is not as sensitive to the measurement location or direction. The C_1 uncertainty was based on axial force uncertainty and hole-to-hole variation for the blind hole calibration tests. This number would be increased to incorporate variation in C_1 with pilot hole diameter if the model was evaluated at these other b_{lim} values.

TABLE 1: Monte Carlo simulation input mean and standard deviation values.

	Mean	**Standard deviation**
k	6×10^7 N/m	20%
f_n	540 Hz	1%
ζ	0.005	20%
C_1	2.69×10^8 N/m^2	10%

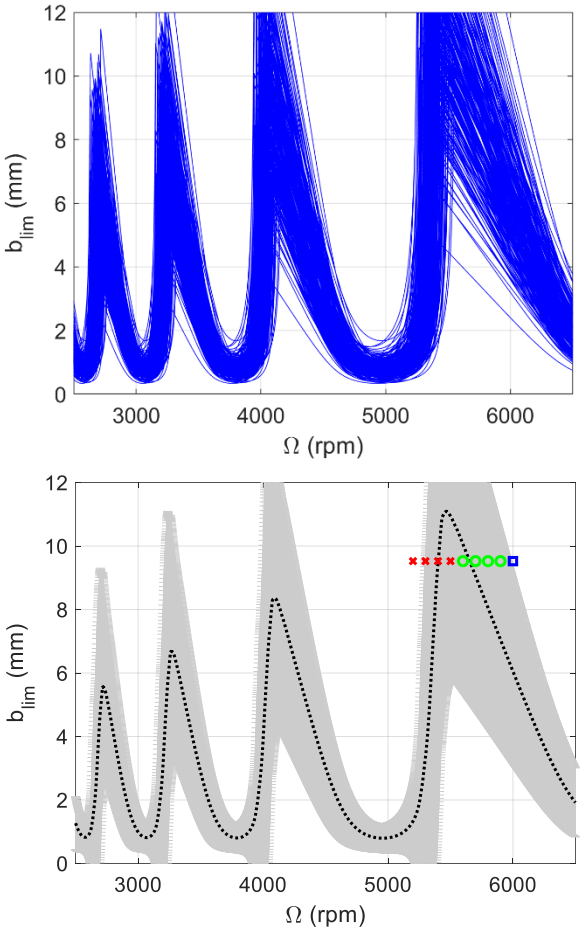

FIGURE 4: Monte Carlo simulations results when varying all four inputs. (Top) 250 stability boundaries obtained by randomly sampling the four inputs from normal distributions. (Bottom) Mean and 95% confidence intervals. Experimental results are included for visual comparison.

Monte Carlo simulation results are displayed in Fig. 4. The top panel shows 250 stability boundaries determined by randomly sampling from independent normal distributions defined by the mean and standard deviation values in Table 1. The four inputs were uncorrelated and generated using the Matlab randn function. Note that C_2 also varied, but was correlated to C_1 since it was calculated using $C_2 = \frac{C_1}{3}$. The bottom panel in Fig. 4 shows the mean and 95% confidence intervals (plus/minus two standard deviations with symmetric error bars) for the stability boundary when varying all four inputs simultaneously. The experimental results are also included. It is seen that all stable cuts are captured within the uncertain boundary; further, the marginal result and two of the four unstable results are outside the boundary.

CONCLUSIONS

In this paper, an uncertainty evaluation for drilling stability was presented using a deterministic frequency-domain drilling stability model. Monte Carlo simulation was used to propagate measurement uncertainties in the model inputs to the output, where the inputs included the modal stiffness, damping ratio, and natural frequency for the torsional-axial vibration mode from the twist drill-holder-spindle axial frequency response function; and the mechanistic coefficients that relate the torque and thrust force to chip area for the selected drill-workpiece material combination. The stability model was used to generate multiple stability maps by randomly sampling from the input distributions. After many iterations, the mean stability boundary and its 95% confidence intervals were determined.

Experimental results for blind hole drilling were presented. It was seen that the deterministic stability boundary obtained from mean input values was qualitatively correct, but shifted in spindle speed. When incorporating the input uncertainties to identify the 95% confidence intervals, all stable results (100%) were captured within the stable zone and the majority of unstable results (3 out of 5) were excluded. Practically, the frequency-domain drilling stability model offers a useful tool for pre-process drilling parameter selection, but conservative choices must be made due to the input uncertainties. The use of Monte Carlo simulation enables the uncertainty in the predicted stability boundary to be evaluated so that improved confidence can be achieved for parameter selection.

ACKNOWLEDGEMENTS

This research was supported by the Korea Institute of Machinery & Materials, DOE Office of Energy Efficiency and Renewable Energy (EERE), Energy and Transportation Science Division, and used resources at the Manufacturing Demonstration Facility, a DOE-EERE User Facility at Oak Ridge National Laboratory. The authors acknowledge contributions by E. Betters to the force modeling.

REFERENCES

[1] Zhang, P.F., Churi, N.J., Pei, Z.J. and Treadwell, C., 2008. Mechanical drilling processes for titanium alloys: A literature review. Machining Science and Technology, 12(4), pp.417-444.

[2] Liu, D., Tang, Y. and Cong, W.L., 2012. A review of mechanical drilling for composite laminates. Composite structures, 94(4), pp.1265-1279.

[3] Abrão, A.M., Faria, P.E., Rubio, J.C., Reis, P. and Davim, J.P., 2007. Drilling of fiber reinforced plastics: A review. Journal of Materials Processing Technology, 186(1-3), pp.1-7.

[4] Pandey, R.K. and Panda, S.S., 2013. Drilling of bone: A comprehensive review. Journal of Clinical Orthopaedics and Trauma, 4(1), pp.15-30.

[5] Xu, J., Mkaddem, A. and El Mansori, M., 2016. Recent advances in drilling hybrid FRP/Ti composite: A state-of-the-art review. Composite Structures, 135, pp.316-338.

[6] Bayly, P.V., Metzler, S.A., Schaut, A.J. and Young, K.A., 2001. Theory of torsional chatter in twist drills: Model, stability analysis and composition to test. Journal of Manufacturing Science and Engineering, 123(4), pp.552-561.

[7] Altıntaş, Y., 2000. Manufacturing Automation. Cambridge: The Press Syndicate of the University of Cambridge.

[8] Schmitz, T. and Smith, K.S., 2019. Machining Dynamics: Frequency Response to Improved Productivity, Second Edition, New York: Springer.

[9] Hodges, D. H., 1980. Torsion of pretwisted beam due to axial loading. ASME Journal of Applied Mechanics, 47, pp.393-397.